Robust and durable aberrative and absorptive phantom for therapeutic ultrasound applications

Alex T. Peek, Gilles P. L. Thomas, Daniel F. Leotta, et al.

ARTICLES YOU MAY BE INTERESTED IN

Robust and durable aberrative and absorptive phantom for therapeutic ultrasound applications

Alex T. Peek,[1] Gilles P. L. Thomas,[1] Daniel F. Leotta,[1] Petr V. Yuldashev,[2] Vera A. Khokhlova,[1,a)] and Tatiana D. Khokhlova[3,b)]

[1]*Center for Industrial and Medical Ultrasound, Applied Physics Laboratory, University of Washington, 1013 NE 40th Street, Seattle, Washington 98105, USA*

[2]*Physics Faculty, Moscow State University, Moscow 119991, Russia*

[3]*Division of Gastroenterology, Department of Medicine, University of Washington, Seattle, Washington 98125, USA*

ABSTRACT:

Phase aberration induced by soft tissue inhomogeneities often complicates high-intensity focused ultrasound (HIFU) therapies by distorting the field and, previously, we designed and fabricated a bilayer gel phantom to reproducibly mimic that effect. A surface pattern containing size scales relevant to inhomogeneities of a porcine body wall was introduced between gel materials with fat- and muscle-like acoustic properties—ballistic and polyvinyl alcohol gels. Here, the phantom design was refined to achieve relevant values of ultrasound absorption and scattering and make it more robust, facilitating frequent handling and use in various experimental arrangements. The fidelity of the interfacial surface of the fabricated phantom to the design was confirmed by three-dimensional ultrasound imaging. The HIFU field distortions—displacement of the focus, enlargement of the focal region, and reduction of focal pressure—produced by the phantom were characterized using hydrophone measurements with a 1.5 MHz 256-element HIFU array and found to be similar to those induced by an *ex vivo* porcine body wall. A phase correction approach was used to mitigate the aberration effect on nonlinear focal waveforms and enable boiling histotripsy treatments through the phantom or body wall. The refined phantom represents a practical tool to explore HIFU therapy systems capabilities. © 2022 Acoustical Society of America. https://doi.org/10.1121/10.0010369

I. INTRODUCTION

High-intensity focused ultrasound (HIFU) has become a rapidly developing technology for noninvasive and minimally invasive therapies.[1–4] HIFU therapies have been used to treat solid tumor targets in many organs, including brain, breast, liver, kidney, and prostate.[5–14] Each organ target presents unique treatment challenges related to its anatomical position. For example, the liver and kidney are located in the abdominal and retroperitoneal cavities, respectively. To reach those targets, the HIFU beam is transmitted through multiple attenuating tissue layers, comprising the inhomogeneous body wall—skin, fascia, fat, muscle, and, in the case of kidney, through a layer of perinephric fat. The difference in the speed of sound, primarily between fat- and water-based tissues, introduces phase aberrations to the beam, resulting in its desynchronization.[15–18] Such an aberration effect is problematic for conventional HIFU therapies as it results in insufficient ultrasound energy delivered to the focus and excess ultrasound energy deposited into adjacent tissues, risking collateral damage. This is particularly critical for newer HIFU technologies that rely on nonlinear

propagation effects as it may prevent or delay a formation of shocks in the acoustic waveform at the focus. Detailed studies of the acoustic aberration effects of human body walls in diagnostic and low energy therapeutic focused ultrasound have previously been reported.[19–23] Approaches for mitigating these effects have been proposed for multielement HIFU arrays and are currently being explored.[24–27] To facilitate the development and testing of these approaches, tissue-mimicking aberrating phantoms would be beneficial because, unlike *ex vivo* animal tissues, they are generally easy to procure or produce, convenient to use, and yield repeatable measurements.

A small number of phantoms that produce acoustic aberrations has been documented.[28–31] Most of these phantoms used a rippled layer of material with a sound speed different from that of water to distort the incident focused beam and were modeled theoretically as a phase screen. The levels of aberration varied according to the design choices, however, the rippled layer was made of rubber or plastic, which had significantly different acoustic properties than the body wall tissues.

Recently, our group has proposed and built an aberration-inducing phantom mimicking a body wall in its effect on linear and nonlinear HIFU fields.[32] The phantom was made of two layers of different materials, replicating the sound speeds in muscle and fat. A rippled interface

---
a)Also at: Physics Faculty, Moscow State University, Moscow 119991, Russia.

b)Also at: Center for Industrial and Medical Ultrasound, Applied Physics Laboratory, University of Washington, 1013 NE 40th Street, Seattle, WA, 98105 USA. Electronic mail: tdk7@uw.edu

between the layers contained a range of spatial frequencies relevant to the porcine body wall. The phantom produced aberration effects similar to those of an *ex vivo* porcine body wall, but ultrasound absorption was much lower and scattering was almost completely absent. Yet, accurate reproduction of acoustic attenuation in the phantom is very important for evaluating the practicality of HIFU imaging guidance methods, aberration correction approaches, and cavitation detection as it affects the signal-to-noise ratio in all of those cases.[24,34] In addition, due to a fragile two-layer design, the phantom was difficult to handle and not robust enough to support frequently repeated measurements.

The goal of this study was to fabricate and characterize an optimized body wall phantom with relevant acoustic attenuation and scattering and robust encapsulated design. The fidelity of the fabricated phantom relative to the original design was evaluated via three-dimensional (3-D) ultrasound imaging. The performance of the phantom was then tested in *ex vivo* HIFU experiments, specifically—boiling histotripsy (BH) exposures of a large volume sample of clotted bovine blood following aberration correction.[33,34]

II. MATERIALS AND METHODS

A. Phantom design and materials

The body-wall-mimicking phantom consisted of a layer of ballistics gel (BG) with a rippled interface for inducing aberrations, fully encased in polyvinyl alcohol (PVA) gel (Fig. 1). PVA and BG were chosen as the base materials because they have sound speeds similar to those of muscle and fat tissues, respectively.[32] These sound speeds were required to produce a realistic aberration effect in the phantom. PVA has a higher sound speed than water ($\sim$1520 m/s) and has previously been used to mimic muscle tissue for acoustic applications.[35,36] BG is a commercial oil-based solid at room temperature with a sound speed lower than that of water ($\sim$1450 m/s) and has been used to mimic fat in our prior aberrating phantom.[32,37,38] In preceding studies, a number of additives have been explored to adjust the acoustic absorption and scattering properties of gel materials, including powder-based and soluble protein and polysaccharide-based agents.[39,40] Soluble organic additives, such as bovine serum albumin, evaporated milk, egg white, and corn syrup, were typically added to phantoms to increase acoustic absorption separately and primarily used in phantoms serving as targets for HIFU thermal ablation.[41–44] Particle-based additives, including graphite, aluminum oxide, glass beads, and silicon dioxide, influence absorption and scattering but also have an effect on the sound speed.[39–42,45] Given that our objective was to introduce the attenuation comparable to that previously reported for the porcine body wall (1.7 dB/cm at 1.5 MHz),[34] yet retain the difference in sound speed between the two materials, we chose to use Al_2O_3 powder following a previously reported recipe of an agar/gelatin phantom.[45,46] In that work, Al_2O_3 powder was chosen over other materials for the following reasons: silicon carbide was cost prohibitive, glass and plastic beads were more challenging to
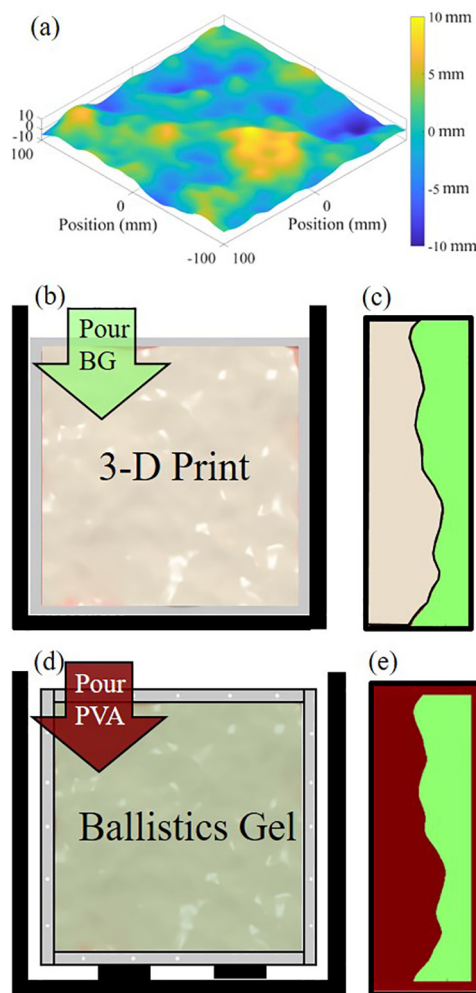

FIG. 1. (Color online) The design and fabrication process to produce the body wall phantom. The (a) surface plot of the phantom's rippled interface containing a range of inhomogeneities relevant to a porcine body wall, (b) 3-D printed mold mounted into metal housing, (c) cross section of BG cast against a 3-D print, (d) patterned BG block mounted into a metal housing with standoff, and (e) cross section of the finished body wall phantom after BG is encapsulated in cured PVA hydrogel are shown.

distribute evenly throughout the gel volume, and graphite particles sank too rapidly before the gel solidified. Further, multiple sizes of Al_2O_3 were used in equal proportion by weight—submicron, 1–2 μm, and 10–40 μm—to create a realistic ultrasound image in terms of uniformity and the size of the speckle. This is consistent with the Food and Drug Administration (FDA) phantom recommended for testing skin surface heating of externally applied ultrasound. The speed of sound in prior work was not significantly affected by the addition of Al_2O_3 powder, and the attenuation was reported to depend linearly on Al_2O_3 concentration within the range of 0%–4%. To attain the targeted attenuation of 1.7 dB/cm at 1.5 MHz, the required concentration of 4% (versus 2% reported previously) was estimated. Another key feature of the phantom was its encapsulated design containing the rippled interfacial surface. Such phantom morphology provided significant physical robustness, which eliminated the need for any support materials.

3008   J. Acoust. Soc. Am. **151** (5), May 2022

Peek *et al.*

First, to facilitate characterization of the acoustic properties of each material, large rectangular 200 mm × 200 mm × 20 mm homogeneous slabs of the PVA and BG materials containing 4% Al_2O_3 powder were produced. Then, the aberrating phantom with dimensions of 200 × 200 × 50 mm was fabricated. The rippled BG block had a thickness of 10–30 mm with an average thickness of 20 mm. This variation in the thicknesses of the two gel materials created a variation in the acoustic travel time across the phantom. Constituent parts of an incident acoustic beam took different paths to the focus, which resulted in aberration.

The mathematical design of the rippled interfacial surface [Fig. 1(a)] was created with the method of random Fourier modes, which has previously been used to model distortions in random media.[47] The full details of the surface design were reported in our previous study, thus, only the essential details are included here. Briefly, a range of spatial harmonics relevant to anatomical feature sizes in a porcine body wall was imbued into the surface. A two-dimensional (2-D) power spectrum $G(k)$ was defined as

$$G(k) = G_0 \frac{\exp\left(\dfrac{-k^2 l_0^2}{2}\right)}{\left(1 + k^2 L_0^2\right)^{11/6}}, \tag{1}$$

where k is a wavenumber such that $k = \sqrt{k_x^2 + k_y^2}$ and $G_0 = G(0)$ scales the surface height to $+/-10$ mm; l_0 and L_0 represent the characteristic small and large scales, respectively, of the features of the interface. The spectrum $G(k)$ was populated with anatomically relevant spatial scales by appropriate choices for l_0 and L_0.[47] The small scale, $l_0 = 5$ mm, was chosen to represent undulations at the tissue–fat interface, and the large scale, $L_0 = 20$ mm, was chosen to represent lobes of fat tapering off into muscle tissues.[34] Notably, Hinkelman and Mast have previously reported similar sizes of distortion-inducing inhomogeneities in human body walls.[19,20] The spectrum $G(k)$ was effectively randomized by combining it with a random complex function $\xi(k_x, k_y) = \xi' + i\xi''$, where the quantities ξ' and ξ'' are real random numbers selected from a pseudorandom Gaussian distribution with zero mean value and unit dispersion,

$$\eta(k_x, k_y) = \xi(k_x, k_y)\sqrt{G(k)}. \tag{2}$$

Finally, an inverse 2-D discrete Fourier transform was performed on the function $\eta(k_x, k_y)$ to obtain the surface.

B. Phantom fabrication

Two rectangular homogeneous slabs of the PVA and BG materials with aluminum oxide powder additives were produced to characterize their acoustic properties. An Al_2O_3 powder was distributed equally by weight among three particle sizes following a previously reported recipe:[45,46] submicron, 1–2 μm, and 10–40 μm (AL600, AL601, AL 602; Atlantic

Equipment Engineers, Bergenfield, NJ) for both slabs. To make the PVA slab, 10% by weight of the PVA powder (99+% hydrolyzed, 89–98 kDa; Sigma-Aldrich, St. Louis, MO) plus 4% by weight of Al_2O_3 powder were added to water and degassed in a vacuum chamber at −685 Torr for 1 h. The solution was heated slowly to 95 °C, then poured into a rectangular steel mold and subsequently frozen for 24 h to cure. The slab was thawed at room temperature and then the freeze-thaw procedure was repeated for a total of three freeze-thaw cycles.[35,36] BG was purchased directly from the manufacturer [Clear Ballistics gelatin (10%); Clear Ballistics, Greenville, SC]. The BG block was melted and degassed at 150 °C, −750 Torr inside a vacuum oven for 12 h (AccuTemp 0.9, Across International, Livingston, NJ). Then, 4% by weight of Al_2O_3 powder was mixed into the BG melt.

The body wall phantom (Fig. 1) was fabricated using a multistep procedure. First, a heat resistant acrylonitrile butadiene styrene (ABS)-like material (ABS Tough, EnvisionTec, Dearborn, MI) was 3-D printed [Fig. 1(b)] into a rectangular shape with the designed rippled surface on one side. The 3-D printed block was placed into a metal mold, and molten BG with 4% Al_2O_3 was poured into the mold and degassed for 48 h at 150 °C and -750 Torr in the vacuum oven. After cooling, the BG piece was peeled away from the 3-D printed part. Two thin metal braces were attached to the outer rim of the imprinted BG piece to precisely mount and position the patterned BG. The BG was mounted into another metal mold as shown in Fig. 1(c). A solution of PVA with 4% Al_2O_3 was poured into the mold, enveloping the BG. The metal mold was put through three freeze-thaw cycles to cure the PVA. The final dimensions of the phantom were approximately 200 × 200 × 50 mm. For comparing the aberration and attenuation effects on nonlinear beam focusing, a freshly excised porcine body wall section with a thickness ranging from 25 to 45 mm was prepared in a thin saline-filled plastic bag.

C. Acoustic characterization of phantom materials

The speed of sound (c) and attenuation coefficient (α) of the homogeneous PVA + Al_2O_3 and BG + Al_2O_3 slabs were measured at the frequencies $f = 1$, 1.5, and 2 MHz with an insertion-loss technique, sometimes referred to as a substitution technique.[36,48] Briefly, the acoustic properties of a material were determined by comparison with a chosen reference material (water). Homogeneous rectangular BG and PVA slabs were submerged in degassed water for several hours prior to the measurement to remove air bubbles.

A flat, unfocused broadband transducer (12.7 mm diameter; Olympus, Center Valley, PA) with 1 MHz central frequency was mounted in a degassed water tank (20 °C, O₂ levels below 15% saturation). The transducer was powered by a function generator (33500B; Keysight Technologies, Inc., Santa Rosa, CA) in series with a linear radio frequency (RF) amplifier (300 W, ENI A-300; ENI, Rochester, NY). A PVDF (polyvinylidene fluoride) capsule hydrophone (HGL-0200 with AH-2020 preamplifier; Onda Corp., Sunnyvale, CA) was attached to a 3-D positioning stage (Velmex, Inc.,

J. Acoust. Soc. Am. **151** (5), May 2022

Peek *et al.* 3009

Bloomfield, NY). The hydrophone was positioned 75 mm away from the transducer and aligned with the transducer's primary axis. This distance was beyond the far-field criterion of $a^2/\lambda = 54$ mm. Here, a is the transducer radius and λ is the ultrasonic wavelength in water at 2 MHz, which yields the furthest far-field distance criterion in our parameter set.[36]

Twenty-cycle waveforms were acquired in the free field and after propagating through the inserted homogeneous slabs. Hydrophone readings were sampled at 2 Gs/s, saved and averaged 512 times with an oscilloscope (DSO-X 3034A; Keysight Technologies, Inc., Santa Rosa, CA). Three steady state cycles of the waveform were isolated, and the harmonic amplitude was determined from the fast Fourier transform (FFT) spectrum. Acquisitions through three different lateral positions of the slabs were used.

The waveforms were analyzed for the sound speed (c) and attenuation coefficient [$\alpha(f)$] at $f = 1$, 1.5, and 2 MHz. The speed of sound, c, was estimated with a time-of-flight calculation. The time shift between the waveforms (Δt) and measured slab thickness (h) were used to directly calculate the sound speed of the slab material such that

$$c_{\text{gel}} = \frac{h}{\Delta t + h/c_{\text{water}}}. \qquad (3)$$

The slab thickness was measured with precision calipers in four positions and averaged: $h = 1.89 \pm 0.01$ cm for both slabs. The thickness measurement in only four points was deemed to be sufficient as the slabs were cast out of a rigid metal mold and, thus, the deviations from the flat surface across the face of the phantom were expected to be small. The attenuation coefficient in units of Np/cm was calculated using the processed hydrophone voltages (V),

$$\alpha(f)_{\text{gel}} = -\frac{1}{h}\ln\left(\frac{V_{\text{gel}}}{V_{\text{water}}}\right), \qquad (4)$$

where V_{water} and V_{gel} are peak hydrophone voltages from the free field and through-slab measurements, respectively. Each of the three measurements acquired at different lateral positions produced a numerical value for c and $\alpha(f)$ for each slab and for all three considered frequencies. The reported values are the average of the three measurements, and the reported error is three times the standard deviation.

The density of the phantom materials was measured directly by executing a volume displacement measurement in a graduated cylinder and a mass measurement with an electronic scale. Thin strips of homogeneous material (approximately 25 g) were prepared and placed in a 50 ml graduated cylinder to maintain low levels of volume uncertainty (± 0.5 ml) in the density values. The reported density is the average of three samples and the error is the result of propagating the volume uncertainty.

The acoustic impedances of the PVA and BG materials were calculated based on the measured density and sound speed. The reflection coefficient was then calculated to be 0.9% for the BG–water interface and 0.2% for the

PVA–water interface using the difference in impedance values and assuming normal incidence in a plane wave regime. The reflections for the assembled body wall phantom were calculated in the same manner with consideration of all interfaces, yielding a total reflection coefficient of 3.9%. These estimated reflections are small relative to the absorption and aberration effects of the phantom and will not be discussed in further detail.

D. 3-D ultrasound scanning evaluation of the phantom

The body wall phantom was scanned with a custom 3-D ultrasound imaging system to verify the accurate reproduction of the rippled interfacial surface. The 3-D imaging system uses a magnetic tracking system (Flock of Birds; Ascension Technology Corp., Burlington, VT) to record the spatial location and orientation of a series of captured 2-D ultrasound images.[49] The phantom was submerged in a large water tank, and a high-frequency linear imaging probe (L12–5, HDI 5000; Philips Ultrasound, Bothell, WA) was manually scanned along a series of parallel paths with a 38-mm image field of view with lateral overlap over the phantom surface. The 2-D images were reformatted into a 3-D gray-scale volume based on the 3-D position and orientation of each image.[50] A total of 4740 2-D images were acquired, and an isotropic volume of $283 \times 281 \times 100$ voxels was reconstructed at 1-mm resolution. The echo interface of the aberrating layer was manually outlined at 4-mm steps in the reconstructed volume data,[49] and the outlines were processed to create a 3-D mesh reconstruction of the aberrating layer surface.[51]

The results of the 3-D reconstruction were used to compare the physical interfacial surface and its associated length scales to the mathematical model. To facilitate a direct comparison between the physical and modeled surfaces, the experimentally reconstructed surface was cropped to 140 mm $\times$ 140 mm to remove extraneous artifacts. The reconstructed surface was then transformed to the modeled surface coordinates centered at (0,0) by using the highest point on the surface as a common reference position. Next, the reconstructed surface was interpolated to match the resolution of the modeled surface of a 0.3 mm step size. Finally, a 2-D FFT was performed for the scanned and modeled surfaces to visualize the distribution of spatial scales.

E. Linear and nonlinear hydrophone measurements with a 256-element focused array

Attenuation and aberration effects produced by the body wall phantom were characterized via hydrophone measurements of the acoustic fields generated by a HIFU array. An excised section of the porcine body wall was characterized in the same fashion to facilitate comparisons. A 256-element spiral HIFU array (Imasonic, Voray sur l'Ognon, France), described in detail elsewhere,[52] was driven and controlled by a research ultrasound system (V1; Verasonics, Ltd., Kirkland, WA). The HIFU array had a 144-mm aperture, 120-mm focal length ($F\# = 0.83$), and operated at a

3010   J. Acoust. Soc. Am. **151** (5), May 2022

Peek *et al.*

1.5 MHz frequency. The array was mounted in a water tank and submerged in degassed water (20 °C, 10% dissolved O_2). A hydrophone was mounted to a 3-D positioning stage to conduct field characterization measurements with and without the phantom or porcine body wall in the propagation path. A fiducial marking on the surface of the phantom allowed for repeatable positioning of the phantom relative to the HIFU array. For measurements at a low power, linear propagation regime, a 75-μm aperture PVDF needle hydrophone (Precision Acoustics, Dorchester, UK) was used. For high power, nonlinear propagation regime, a fiber optic hydrophone was used (FOPH2000, 100-μm fiber tip diameter, 100-MHz bandwidth; RP Acoustics, Leutenbach, Germany).

In the linear regime, the acoustic field measurements were performed with and without the phantom or body wall inserted in front of the HIFU transducer. In all three cases, the PVDF hydrophone was moved to the position of the maximum pressure amplitude, which we will be referred as the focus throughout the paper, and a transverse 2-D scan of dimensions 30 mm × 30 mm was performed. The focus shift in the axial and transverse directions was measured and the distortion produced by aberration was estimated by comparison of -6 dB dimensions of the beam area.

In the nonlinear regime, focal pressure waveforms were collected across the full range of the HIFU system drive voltage with and without the phantom or body wall inserted. In all three cases, the fiber optic hydrophone was moved to the location of the highest peak positive pressure in the 3-D space at a drive voltage corresponding to a fully developed shock.[53] This position will be referred to as the nonlinear focus throughout. The displacement of the nonlinear focus on insertion of the phantom or body wall and the change in its magnitude value were recorded.

In a subset of nonlinear measurements, a phase-aberration correction approach developed for the HIFU array was used.[24] Briefly, the array was operated in a pulse-echo mode at a drive voltage corresponding to moderate nonlinear distortion of the focal free field waveform. The hydrophone tip positioned at the nonlinear focus was used as a point reflector, and its echo was received on each of the 256 elements. To mitigate aberrations, an appropriate phase correction for each element was found using cross correlation of the received echoes and was then applied to the array. The resulting phase correction rectified waveform aberrations near the focus and restored shock-forming behavior at nonlinear drive levels. Note that while here the backscattering from the tip of the FOPH hydrophone—a strong point reflector—was used to perform the correction, to fully characterize the effects of the phantom itself, the approach has already been demonstrated to work well with diffuse backscatter from tissue, *ex vivo* and *in vivo*, in pigs.[24,54]

The attenuation effects of the phantom and body wall were estimated using a derating technique developed for nonlinear focused beams, assuming that nonlinearity coefficients of the phantoms are equal to that of water.[55] The

system drive voltage, V, was scaled linearly to compensate for prefocal attenuation affording a comparison between waveforms measured in the free field and behind the phantom or body wall with aberration correction.[24] Using the phantom case as an example, the corresponding scaling factor, $V_{water}/V_{phantom}$, was calculated using the ratio of pressure amplitudes, $P_{phantom}/P_{water}$, measured at the corresponding focus positions at the lowest driving voltage (linear regime),

$$\frac{P_{phantom}}{P_{water}} = \frac{V_{water}}{V_{phantom}} = \exp\big(-\alpha(f)_{phantom}\big). \tag{5}$$

F. Example BH treatment

Following the hydrophone-facilitated measurement of phantom-induced aberration, the phantom was tested in the context of an *ex vivo* BH HIFU treatment. After the aberration correction was applied to the array, the fiber optic hydrophone was replaced with a large bovine blood clot of about 100 mm × 60 mm × 30 mm dimensions. The HIFU focus was placed 15 mm below the proximal face of the clot. This tissue model has previously been used as a target for HIFU therapies due to its homogeneity and ease of use, combined with acoustic properties that are similar to those of the liver and kidney.[24,56,57] The bovine blood was procured from a local abattoir and stabilized with a 1:9 ratio of citrate-based anticoagulant. The blood was degassed in a vacuum chamber for 1 h at -680 Torr and subsequently poured into a thin plastic bag. A $CaCl_2$ solution was added to a concentration of 25 mM to clot the blood.[57] B-mode videos of the treatment were recorded with an inline ultrasound imaging probe (P6–3; ATL, Bothell, WA).

The BH threshold was roughly determined by increasing the system voltage in 10 V increments and emitting isolated 10 ms pulses until a hyperechoic region in the clot was observed on B-mode ultrasound, indicating initiation of bubble activity. This threshold amplitude was used to deliver another 30 pulses at 1 Hz pulse repetition frequency (PRF) to the clot to produce a BH lesion. Following treatment, the clot sample was bisected and photographed.

III. RESULTS

A. Practical features of the body wall phantom

As the primary purpose of refining the original design of the body wall phantom was to help develop preclinical HIFU exposures, we focus here on its key practical features: ease of use and repeatability. The developed phantom was physically robust and could be easily mounted to a water tank using optical posts or placed on top of a target tissue sample in a "dry" setting. The encapsulated design of the phantom has removed the need for additional acoustic window support materials such as Mylar used in the previous design.[32] Eliminating the acoustic window material was beneficial because the windows could sag, crease, or become damaged over time, as well as trap bubbles between the interfaces. The phantom's 200 mm × 200 mm usable

J. Acoust. Soc. Am. **151** (5), May 2022
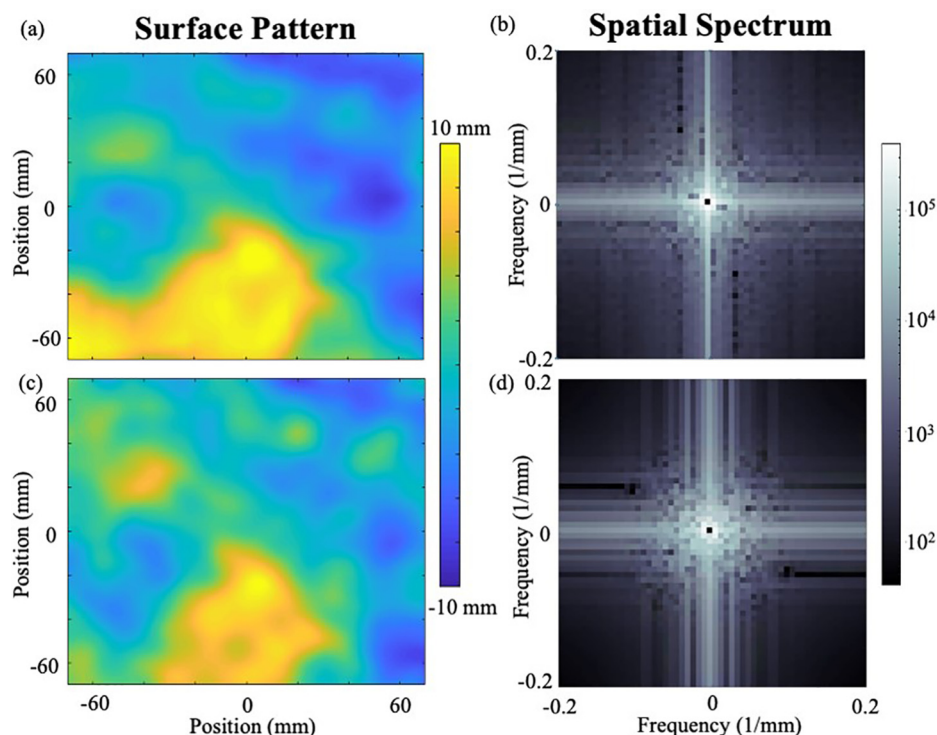
Peek *et al.*   3011

FIG. 2. (Color online) The characterization of the body wall phantom's rippled interfacial surface via 3-D ultrasound imaging. The (a) reconstruction of the interfacial surface, (b) 2-D frequency domain plot of the reconstructed surface, (c) surface plot of the mathematical interfacial surface, and (d) 2-D frequency domain plot of the mathematical surface are shown.

area gave access to several different sites to test somewhat different aberration levels.[32]

Several design features improved the repeatability of the measurements with the phantom and its longevity. The internal metal brace and external mounting bar robustly supported the phantom and attached it to fixtures used in the experiments. This rigidity ensured that the phantom did not distort its shape or slump over time. The brace was designed to hold the BG layer perpendicular to the acoustic axis and avoid complications of angled interfaces. A fiducial marker on the surface of the phantom allowed the user to position the phantom accurately. The phantom was stored in deionized (DI) water with 0.1% Dettol antiseptic and has shown very little physical degradation after 12 months. Specifically, the phantom has been imaged with an ultrasound probe each time it was used in experiments throughout the year (1–4 times per month, on average) to assess the presence of sloughing and the accumulation of water between the gel layers, presence of bacterial growth, and associated formation of bubbles and changes in reflectance, as well as a visual assessment of the integrity and smoothness of the outer layers. No changes were detected. The metal bracing and mounting structure had not moved relative to the gel layers and remained robustly attached to them. Several phantom replicas have since been fabricated using the same 3-D printed mold.

B. 3-D scanning validation of body wall phantom

The interfacial surface patterns and corresponding 2-D spatial spectra of the phantom reconstructed from the 3-D ultrasound imaging and initial computational model are shown in Fig. 2. The average difference in height between the modeled and measured surfaces [Figs. 2(a) and 2(c), respectively] was 0.33 mm and the standard deviation was 2.8 mm, which suggested that the interfacial surface was replicated with excellent fidelity. The spatial frequencies of the rippled surface are critical to replicate the acoustic properties of a real porcine body wall. For the reconstructed surface, these frequencies were calculated directly with a 2-D Fourier transform and plotted along with the originally designed transform on a logarithmic scale in Figs. 2(b) and 2(d). Overall, the similarity in the spatial spectra of the modeled and reconstructed surface can be visually appreciated.

C. Acoustic properties of phantom materials

The measured sound speeds (c), densities (ρ), and attenuation coefficients (α) of the homogenous PVA and BG slabs are listed in Table I. The literature values for the corresponding porcine tissues are also included in Table I. Importantly, the sound speed of the Al_2O_3-containing PVA

TABLE I. The sound speed, density, and attenuation coefficients at 1.5 MHz for tissue-mimicking gels and soft porcine tissues. Three different lateral positions were used to measure the sound speed and attenuation. Three samples were used to calculate the density of BG and PVA.

Material	Sound speed (m/s)	Density (kg/m³)	Attenuation (dB/cm)
BG[a]	1439 ± 3.6	854 ± 11	1.56 ± 0.07
PVA[a]	1524 ± 3.6	1060 ± 24	1.63 ± 0.01
Porcine fat (Refs. 58 and 59)	1426–1470	870	2.4–4.0
Porcine muscle (Refs. 56, 60, and 61)	1579–1620	1040–1100	1.2–1.8

[a]Measured values from this study.

3012   J. Acoust. Soc. Am. **151** (5), May 2022
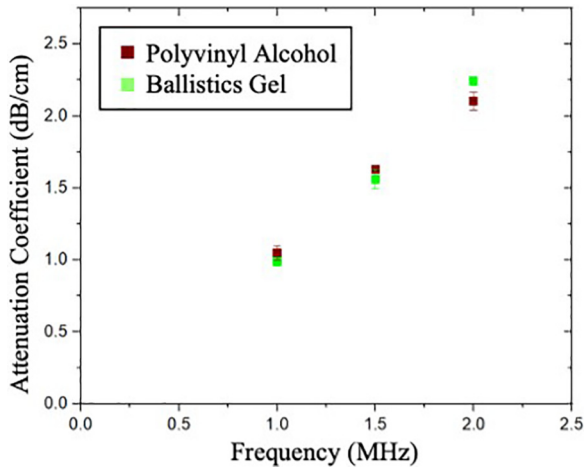
Peek *et al.*

FIG. 3. (Color online) The attenuation coefficient measurement of PVA and BG versus the frequency.

and BG materials were found to be within 1% of those previously reported by the authors in pure PVA and BG and close to their tissue counterparts to generate realistic aberrations.[32] Similarly, the densities and, therefore the acoustic impedances were close to those of the fat and muscle tissues.

The attenuation coefficients measured at 1, 1.5, and 2 MHz in homogeneous slabs of phantom materials are plotted in Fig. 3. The measured values were matched reasonably well with their real porcine tissue counterparts of fat and muscle. The attenuation in fat was reported to be somewhat higher than that in BG with 4% Al_2O_3, which theoretically be improved on by adding a higher concentration of Al_2O_3. However, even the 4% concentration used here was already at the brink of practically achievable for the BG material while ensuring homogenous distribution of the particles. Furthermore, the ultimate goal in developing this phantom was to match the overall attenuation of the body wall previously encountered by the authors experimentally[34]—1.3 dB/cm at 1.5 MHz—rather than the attenuations and relative thicknesses of its components—muscle and fat. The total attenuation of the phantom can be estimated assuming an average thickness of 2 cm for the BG gel and 3 cm for the PVA gel, which yields 8.0 dB at 1.5 MHz, or 1.6 dB/cm average attenuation coefficient. Such values represents a "worst-case" attenuation level that would be reasonable for a real porcine body wall.[34]

D. Distortions of the linear acoustic field

Low amplitude 2-D pressure fields corresponding to propagation through water, the body wall phantom, and a section of excised porcine body wall are compared in Fig. 4. In all cases, the zero coordinate is positioned at the focus, i.e., the maximum pressure amplitude. Two metrics considered for comparison are the −6 dB beam area and reduction in the pressure maximum. The body wall phantom produced a strong distortion of the linear field as shown in Fig. 4(b). The −6 dB area of the focal 2-D transverse field increased from 0.81 mm² in the free field to 8.75 mm² behind the phantom. The maximum pressure amplitude behind the phantom was reduced to 22% of the free field value.

The isolated effect of aberration on the maximum pressure amplitude can be estimated using the measured material attenuation properties. It would be reduced to 39% of the value in the free field due to attenuation alone. Thus, the effect of aberration nearly doubled the overall pressure amplitude loss at the focus.

The distortion to the acoustic field around the focus caused by the excised porcine body wall is shown in Fig. 4(c). The −6 dB area changed from 0.81 mm² in the free field to 2.8 mm² behind the body wall. The focal pressure behind the body wall was reduced to 44% of the free field value. The reduction in pressure due to aberration alone could not be isolated in this case because the geometry of the body wall and its constituent material properties were not known. The body wall phantom exceeded the overall amplitude reduction and focal beam spreading produced by the body wall.

E. Nonlinear acoustic field measurement results

Nonlinear focal waveforms were collected with and without the body wall phantom or porcine body wall inserted and centered on the transducer beam axis. The inserted phantom or body wall shifted the position of the nonlinear focus, which corresponded to the position of a fully shocked waveform in the free field. Referencing the coordinate system in Fig. 4, insertion of the phantom moved the nonlinear focus to coordinates {0.48 mm, 0.2 mm, 0.4 mm}, where the last coordinate refers to the Z axis, which is the HIFU acoustic axis. The insertion of the body wall moved the nonlinear focus to coordinates {0.1 mm, 0.35 mm, 3.05 mm}.
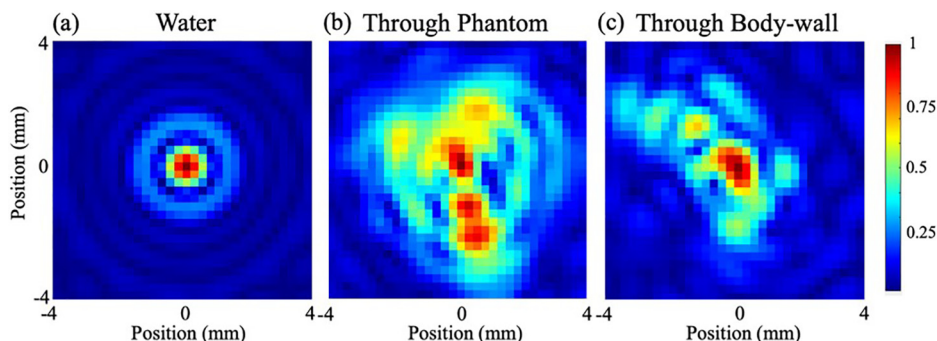

FIG. 4. (Color online) The measured linear 2-D pressure amplitude distributions acquired in the focal plane are depicted in (a) the free field (water), (b) with the aberrating body wall phantom inserted, and (c) with the porcine body wall inserted. The pressure amplitudes are normalized to the maximum pressure value in each plot.

J. Acoust. Soc. Am. **151** (5), May 2022

Peek *et al.*   3013

Following the hydrophone measurements at the nonlinear focus behind the body wall phantom and porcine body wall section, the phase corrections to mitigate aberration were found for each of the 256 elements of the array using the pulse-echo method. Figure 5 shows a map of the transducer elements with the phase correction applied for the two cases. The phase correction for the phantom case ranged from approximately π to $-\pi/2$; the phase correction to the body wall case ranged from approximately π to -π. In both cases, the distributions and sizes of the areas with similar phases were similar, suggesting comparable phase aberration by the phantom and body wall. For phase-aberration correction algorithms that involve the cross correlation of backscattered signals from pairs of nearest neighbor elements,[24] the phase difference variability across pairs of elements is of interest, and in present case, it had a mean and standard deviation of 0.33 ± 0.27 rad, and 0.45 ± 0.3 rad for the phantom and body wall, respectively.

Pressure waveforms were recorded at the positions of the nonlinear focus in the free field and behind the phantom and body wall across a range of system voltages with and without aberration correction to facilitate quantitative comparisons. Figures 6(a) and 6(b) show the dependences of the peak focal pressures on system driving voltage in the free field and behind the phantom and body wall with and without aberration correction. As expected, aberration corrections in both cases have a much larger impact on the peak positive pressures (286% and 256% maximum for the body wall and phantom, correspondingly) compared to the peak negative pressures (189% and 160% maximum, correspondingly) and in the nonlinear propagation regimes (i.e., at higher driving voltages) compared to the linear regime. For example, Fig. 6(c) shows that aberration correction in the regime of fully developed shocks (34 V) increased the focal peak positive pressure from 34 MPa to 86 MPa for the phantom case and from 36 MPa to 103 MPa for the body wall case. For the phantom and body wall, the waveform was restored to a fully shocked state, which would be critically important for the shock-wave dependent HIFU therapies such as shock-scattering, hybrid, and BH.

The attenuation of the phantom and body wall was estimated using the method of derating developed for focused

FIG. 6. (Color online) The (a) peak positive and (b) peak negative pressures measured in nonlinear focus versus the *v*oltage, including free field data, aberration-corrected, and uncorrected data sets behind the phantom and body wall, as well as (c) the focal waveforms acquired at high drive level (34 V) through the aberrating phantom and porcine body wall with and without aberration correction are shown. Arbitrary phases were added to the waveforms to improve visualization.

nonlinear fields.[46] The driving voltages corresponding to the waveforms measured in nonlinear focus behind the phantom and body wall with aberration correction were linearly scaled by the amount related to the inserted material's attenuation using Eq. (5) as described in Sec. II E. Specifically, the voltage levels for the focal waveforms behind the phantom and body wall were reduced by the derating factor, $V_{water}/V_{phantom}$, and $V_{water}/V_{body\,wall}$. In this way, a voltage-scaled waveform behind the phantom would be nearly
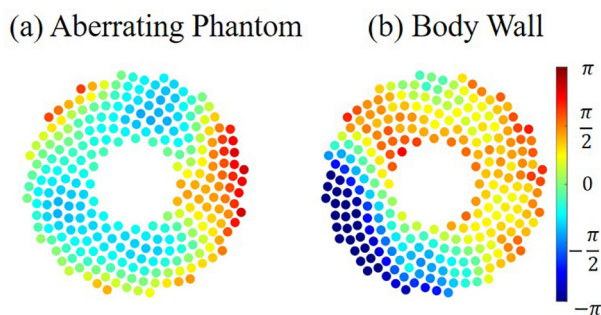

FIG. 5. (Color online) The phase correction applied to each of the 256 elements on the HIFU transducer in the cases of the (a) aberrating phantom and (b) porcine body wall are shown.
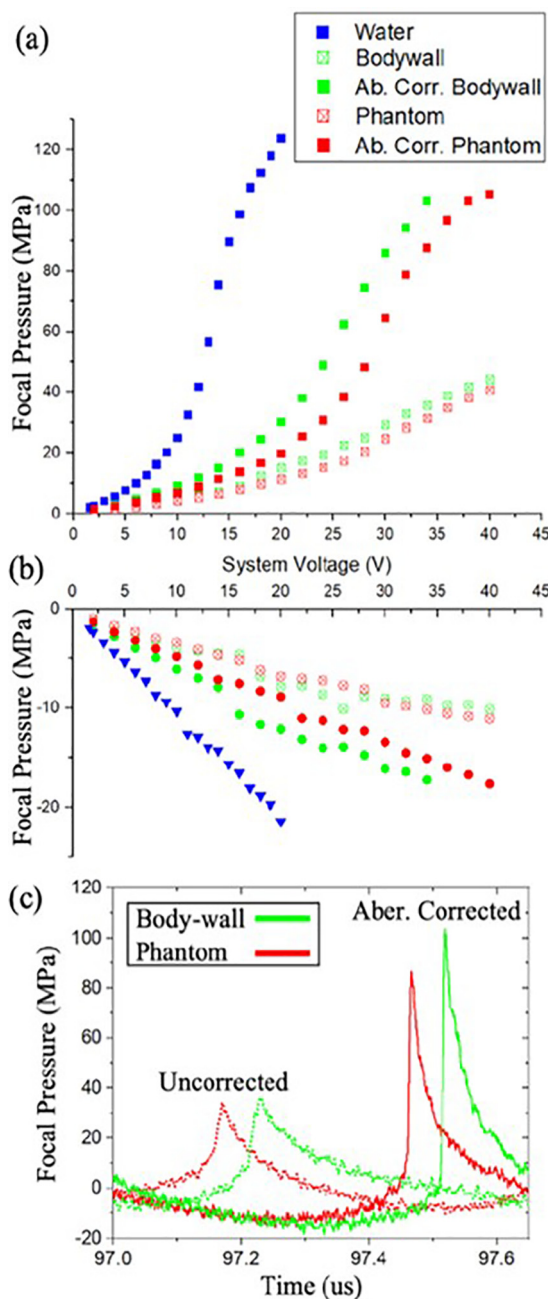
equivalent to a focal waveform under free field conditions. The derating factors, $V_{water}/V_{phantom} = 0.45$ and $V_{water}/V_{body\,wall} = 0.54$, were determined using the ratio of focal pressure amplitudes in water and behind the phantom or body wall at the lowest drive level. The free field and derated pressures in nonlinear focus are plotted against system voltages in Figs. 7(a) and 7(b), respectively. The corresponding total attenuation levels were extracted per Eq. (5) and are additionally reported normalized to the total material thickness: $\alpha_{phantom} = 6.9\,dB$ (1.4 dB/cm) and $\alpha_{body\,wall} = 5.2\,dB$ (1.3 dB/cm). The estimated total attenuation of the phantom using the measured material properties was 8.0 dB (1.6 dB/cm). This discrepancy between the attenuation values of the phantom translates to a 5% difference in the pressure amplitude through the phantom in the linear regime. The estimated attenuation of the body wall was previously unknown but was reasonable given the attenuation of the fat and muscle components and the estimated thickness of 4 cm using ultrasound images. The overall attenuation of the body wall was lower than that of the phantom primarily due to the thickness of the specimen.

F. BH treatment through the phantom

The feasibility of the BH treatment of clotted bovine blood through the body-wall-mimicking phantom and porcine body wall were evaluated and compared. Following the aberration correction described above, the clotted bovine blood sample replaced the fiber optic hydrophone as shown in Figs. 8(a) and 8(d). This *ex vivo* configuration was analogous to the geometric arrangement for the ablation of porcine liver *in vivo*.[34] For the phantom and body wall cases, BH was initiated at a 40 V drive level. The shock amplitude behind the phantom measured at 40 V was 104 MPa. Neglecting the attenuation inside the blood clot, the time to reach boiling could be estimated per the weak shock theory as 2.2 ms.[33] The shock amplitude measured behind the body wall at 34 V (the highest voltage waveform recorded) was
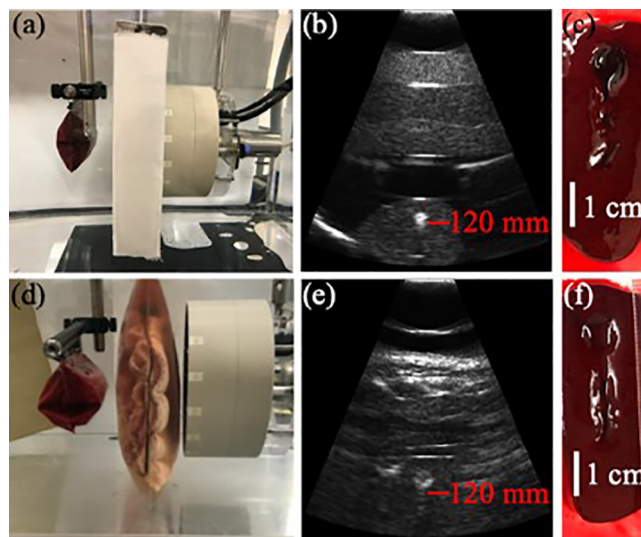
FIG. 8. (Color online) An overview of the BH treatment. The treatment setup included the HIFU array, organ-mimicking phantom, and inserted (a) aberrating phantom or (d) body wall. The B-mode images from the end of the 30 s treatment indicated bubble activity in the focal region for the (b) phantom and (e) body wall cases. The resulting lesions in the organ-mimicking phantom are shown for the (c) phantom and (f) body wall cases.

102 MPa, corresponding to a similar time-to-boil. These shock amplitudes would be expected to produce BH activity in the clot based on our previous studies.[57] Cross sections of the clot after delivering 30 BH pulses showed the liquefied lesion area for the phantom case [28 mm × 8 mm; Fig. 8(c)] and body wall case [30 mm × 9 mm; Fig. 8(f)]. Without aberration correction, BH treatments were not possible in the tested samples.

IV. DISCUSSION AND CONCLUSIONS

HIFU ablation of most abdominal and retroperitoneal targets is complicated by attenuation and phase aberration induced primarily by fat. These effects are especially important to consider and mitigate in HIFU treatments that rely on the formation of shock fronts at the focus—shock-enhanced thermal ablation, shock-scattering histotripsy, and BH.[4,33,34] A durable and robust gel phantom that would mimic aberration and attenuation of a porcine body wall would serve as a very useful tool in developing HIFU techniques. In this study, such a phantom was fabricated, characterized, and tested. The study builds on our previous version[32] of a similar aberrating phantom with several major improvements to the phantom design and characterization. Improvements included a robust encapsulated-phantom design, 3-D ultrasound mapping of the fabricated phantom to confirm its fidelity, tuned gel materials to match the attenuation of porcine tissues, and aberration correction methods. The phantom performance was tested by separately characterizing aberration and attenuation effects on linear and nonlinear HIFU fields and comparing these effects to those imposed by a porcine body wall. Further, the phantom was used in a practical scenario of facilitating a realistic *ex vivo* BH treatment.
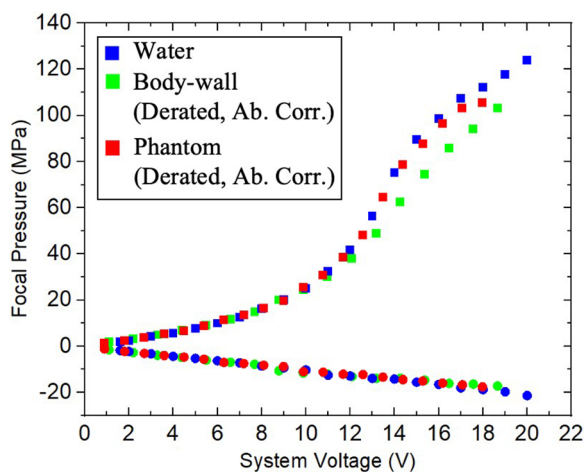

FIG. 7. (Color online) The measurements of the peak positive and peak negative focal pressures versus the system driving *v*oltage are depicted, including the free field data and derated, aberration-corrected data behind the phantom and body wall.

J. Acoust. Soc. Am. **151** (5), May 2022

Peek *et al.* 3015

The body wall phantom was fabricated with a robust encapsulated design, which eliminated the need for acoustic window supports as were required in the previous version of the phantom. This made the phantom easy to use and resistant to degradation, such as slumping. Per the 3-D ultrasound mapping of the rippled surface in the fabricated phantom, it matched the originally designed surface with high accuracy with the difference being 0.3 mm on average. Selected gel materials matched the properties of the porcine fat and muscle tissues so that the phantom could produce realistic attenuation and aberration levels of a body wall. Inclusion of Al_2O_3 powder in the gel materials to tune their attenuation represented an important improvement over our previous phantom, which used low attenuation materials.

Hydrophone mapping of the HIFU field behind the phantom and *ex vivo* porcine body wall at low output power (linear propagation regime) allowed for comparing the aberration induced distortion of the focus. Qualitatively, the distortion induced by the phantom was similar to that induced by the body wall, although quantitatively the focus shift and focus spreading, defined as the focus area at the -6 dB level, were larger behind the phantom but still within a reasonably expected range.

Because the primary purpose of the fabricated phantom is to facilitate the investigation of shock-wave HIFU exposures, the key aspect of this work was to characterize the nonlinear field distortion produced by the phantom. Insertion of the phantom and body wall in the HIFU path significantly reduced focal pressures and eliminated the shock front. An aberration correction technique that used the hydrophone tip as a strong point reflector was employed to adjust the phases of each of the array elements to align the wavefront phases at the focus. The phantom and body wall required phase correction to the array elements from approximately $-\pi$ to $\pi/2$. Application of the aberration correction restored the shock front and high focal pressure (up to 100 MPa shock amplitude) in the phantom and body wall cases, which would be required for shock front HIFU therapies. Additionally, a derating technique was used to estimate the attenuation of the body wall and phantom. The normalized attenuation of the phantom materials (1.4 dB/cm) and body wall components (1.3 dB/cm) were very similar. The total attenuation of the phantom was 33% higher primarily because it was thicker; therefore, the phantom represented a reasonable worst-case scenario.

The isolated effects of aberration and attenuation on the peak focal pressures were compared for the phantom and body wall. The close peak positive pressure values behind the phantom and body wall without aberration correction (e.g., 8.9% difference at 34 V) suggested that the combined effects of aberration and attenuation were similar in the two cases. Comparing peak positive pressure values for the phantom and body wall cases with aberration correction (e.g., 15% difference at 34 V) suggested that the attenuation for both cases was also similar. It can then be inferred that the aberration effects of the phantom and body wall were also similar.

It is worth noting that each set of recorded measurements corresponded to one series of experiments with the same relative position of the transducer array and the phantom or body wall. Repositioning of the phantom in the tank can produce a modestly different distortion of the acoustic field and, consequently, the aberration effect is slightly setup dependent.[32] The aberration and attenuation produced by the body wall would also likely be sample dependent. This work was not meant to cover all possible configurations but to carefully study one representative arrangement.

Finally, a single focus BH treatment was performed through the phantom and body wall inside a blood clot. After a 30 s treatment, large lesions (approximately 30 mm $\times$ 9 mm) were formed. Aberration correction was required to initiate BH, demonstrating the importance of developing phase correction methods for HIFU therapies that the phantom currently facilitates.

ACKNOWLEDGMENTS

[1]C. R. Hill and G. R. ter Haar, "Review article: High intensity focused ultrasound-potential for cancer treatment," Br. J. Radiol. **68**, 1296–1303 (1995).

[2]M. R. Bailey, V. A. Khokhlova, O. A. Sapozhnikov, S. G. Kargl, and L. A. Crum, "Physical mechanisms of the therapeutic effect of ultrasound (a review)," Acoust. Phys. **49**, 369–388 (2003).

[3]T. D. Khokhlova, M. S. Canney, V. A. Khokhlova, O. A. Sapozhnikov, L. A. Crum, and M. R. Bailey, "Controlled tissue emulsification produced by high intensity focused ultrasound shock waves and millisecond boiling," J. Acoust. Soc. Am. **130**, 3498–3510 (2011).

[4]V. A. Khokhlova, J. B. Fowlkes, W. W. Roberts, G. R. Schade, Z. Xu, T. D. Khokhlova, T. L. Hall, A. D. Maxwell, Y. N. Wang, and C. A. Cain, "Histotripsy methods in mechanical disintegration of tissue: Towards clinical applications," Int. J. Hyperthermia **31**, 145–162 (2015).

[5]J. E. Kennedy, "High-intensity focused ultrasound in the treatment of solid tumours," Nat. Rev. Cancer **5**, 321–327 (2005).

[6]W. W. Roberts, "Focused ultrasound ablation of renal and prostate cancer: Current technology and future directions," Urol. Oncol.: Semin. Orig. Invest. **23**, 367–371 (2005).

[7]M. D. Gillett, M. T. Gettman, H. Zincke, and M. L. Blute, "Tissue ablation technologies for localized prostate cancer," Mayo Clinic Proc. **79**, 1547–1555 (2004).

[8]R. O. Illing, J. E. Kennedy, F. Wu, G. R. ter Haar, A. S. Protheroe, P. J. Friend, F. V. Gleeson, D. W. Cranston, R. R. Phillips, and M. R. Middleton, "The safety and feasibility of extracorporeal high-intensity focused ultrasound (HIFU) for the treatment of liver and kidney tumours in a Western population," Br. J. Cancer **93**, 890–895 (2005).

[9]C. G. Chaussy and S. Thuroff, "Transrectal high-intensity focused ultrasound for local treatment of prostate cancer. 2009 Update," Urologe **48**, 710–718 (2009).

[10]C. H. Fernandez, E. L. Garcia, D. S. Rios, and G. B. Chomon, "Conservative treatment of renal cancer using HIFU. Procedure, indications, and results," Actas Urologicas Esp. **33**, 522–525 (2009).

[11]G. J. Vricella, L. E. Ponsky, and J. A. Cadeddu, "Ablative technologies for urologic cancers," Urologic Clinics North Am. **36**, 163–178 (2009).

[12]G. Malietzis, L. Monzon, J. Hand, H. Wasan, E. Leen, M. Abel, A. Muhammad, P. Price, and P. Abel, "High-intensity focused ultrasound: Advances in technology and experimental trials support enhanced utility of focused ultrasound surgery in oncology," Br. J. Radiol. **86**, 20130044 (2013).

3016   J. Acoust. Soc. Am. **151** (5), May 2022

Peek *et al.*

[13]W. H. She, T. T. Cheung, C. R. Jenkins, and M. G. Irwin, "Clinical applications of high-intensity focused ultrasound," Hong Kong Med. J. **22**, 382–392 (2016).

[14]Y. H. Hsiao, S. J. Kuo, H. D. Tsai, M. C. Chou, and G. P. Yeh, "Clinical application of high-intensity focused ultrasound in cancer therapy," J. Cancer **7**, 225–231 (2016).

[15]R. Ritchie, J. Collin, C. Coussios, and T. Leslie, "Attenuation and defocusing during high-intensity focused ultrasound therapy through perinephric fat," Ultrasound Med. Biol. **39**, 1785–1793 (2013).

[16]Z. B. Liu, T. B. Fan, D. Zhang, and X. F. Gong, "Influence of the abdominal wall on the nonlinear propagation of focused therapeutic ultrasound," Chin. Phys. B **18**, 4932–4937 (2009).

[17]T. Christopher, "Finite amplitude distortion-based inhomogeneous pulse echo ultrasonic imaging," IEEE Trans. Ultrason., Ferroelect., Freq. Control **44**, 125–139 (1997).

[18]J. J. Macoskey, T. L. Hall, J. R. Sukovich, S. W. Choi, K. Ives, E. Johnsen, C. A. Cain, and Z. Xu, "Soft-tissue aberration correction for histotripsy," IEEE Trans. Ultrason., Ferroelect., Freq. Control **65**, 2073–2085 (2018).

[19]L. M. Hinkelman, T. D. Mast, L. A. Metlay, and R. C. Waag, "The effect of abdominal wall morphology on ultrasonic pulse distortion. Part I. Measurements," J. Acoust. Soc. Am. **104**, 3635–3649 (1998).

[20]T. D. Mast, L. M. Hinkelman, M. J. Orr, and R. C. Waag, "The effect of abdominal wall morphology on ultrasonic pulse distortion. Part II. Simulations," J. Acoust. Soc. Am. **104**, 3651–3664 (1998).

[21]L. M. Hinkelman, D. L. Liu, L. A. Metlay, and R. C. Waag, "Measurements of ultrasonic pulse arrival time and energy-level variations produced by propagation through abdominal-wall," J. Acoust. Soc. Am. **95**, 530–541 (1994).

[22]T. D. Mast, L. M. Hinkelman, M. J. Orr, V. W. Sparrow, and R. C. Waag, "Simulation of ultrasonic pulse propagation through the abdominal wall," J. Acoust. Soc. Am. **102**, 1177–1190 (1997).

[23]Y. Sumino and R. C. Waag, "Measurements of ultrasonic pulse arrival time differences produced by abdominal-wall specimens," J. Acoust. Soc. Am. **90**, 2924–2930 (1991).

[24]G. P. L. Thomas, T. D. Khokhlova, C. R. Bawiec, A. T. Peek, O. A. Sapozhnikov, M. O'Donnell, and V. A. Khokhlova, "Phase-aberration correction for HIFU therapy using a multielement array and backscattering of nonlinear pulses," IEEE Trans. Ultrason., Ferroelect., Freq. Control **68**, 1040–1050 (2021).

[25]E. Herbert, M. Pernot, G. Montaldo, M. Fink, and M. Tanter, "Energy-based adaptive focusing of waves: Application to noninvasive aberration correction of ultrasonic wavefields," IEEE Trans. Ultrason., Ferroelect., Freq. Control **56**, 2388–2399 (2009).

[26]Y. Hertzberg, A. Volovick, Y. Zur, Y. Medan, S. Vitek, and G. Navon, "Ultrasound focusing using magnetic resonance acoustic radiation force imaging: Application to ultrasound transcranial therapy," Med. Phys. **37**, 2934–2942 (2010).

[27]M. Pernot, G. Montaldo, M. Tanter, and M. Fink, " 'Ultrasonic stars' for time reversal focusing using induced cavitation bubbles," AIP Conf. Proc. **829**, 223–227 (2006).

[28]G. C. Ng, P. D. Freiburger, W. F. Walker, and G. E. Trahey, "A speckle target adaptive imaging technique in the presence of distributed aberrations," IEEE Trans. Ultrason., Ferroelect., Freq. Control **44**, 140–151 (1997).

[29]P. V. Yuldashev, L. M. Krutyansky, V. A. Khokhlova, A. P. Brysev, and F. V. Bunkin, "Distortion of the focused finite amplitude ultrasound beam behind the random phase layer," Acoust. Phys. **56**, 467–474 (2010).

[30]Z. B. Liu, X. S. Guo, J. Tu, and D. Zhang, "Variations in temperature distribution and tissue lesion formation induced by tissue inhomogeneity for therapeutic ultrasound," Ultrasound Med. Biol. **40**, 1857–1868 (2014).

[31]Z. B. Liu, T. B. Fan, X. S. Guo, and D. Zhang, "Effect of tissue inhomogeneity on nonlinear propagation of focused ultrasound," Chin. Phys. Lett. **27**, 094303 (2010).

[32]A. T. Peek, C. Hunter, W. Kreider, T. D. Khokhlova, P. B. Rosnitskiy, P. V. Yuldashev, O. A. Sapozhnikov, and V. A. Khokhlova, "Bilayer aberration-inducing gel phantom for high intensity focused ultrasound applications," J. Acoust. Soc. Am. **148**, 3569–3580 (2020).

[33]M. S. Canney, V. A. Khokhlova, O. V. Bessonova, M. R. Bailey, and L. A. Crum, "Shock-induced heating and millisecond boiling in gels and tissue due to high intensity focused ultrasound," Ultrasound Med. Biol. **36**, 250–267 (2010).

[34]T. D. Khokhlova, G. R. Schade, Y. N. Wang, S. V. Buravkov, V. P. Chernikov, J. C. Simon, F. Starr, A. D. Maxwell, M. R. Bailey, W. Kreider, and V. A. Khokhlova, "Pilot *in vivo* studies on transcutaneous boiling histotripsy in porcine liver and kidney," Sci. Rep. **9**, 20176 (2019).

[35]A. Kharine, S. Manohar, R. Seeton, R. G. M. Kolkman, R. A. Bolt, W. Steenbergen, and F. F. M. de Mul, "Poly(vinyl alcohol) gels for use as tissue phantoms in photoacoustic mammography," Phys. Med. Biol. **48**, 357–370 (2003).

[36]K. J. M. Surry, H. J. B. Austin, A. Fenster, and T. M. Peters, "Poly(vinyl alcohol) cryogel phantoms for use in ultrasound and MR imaging," Phys. Med. Biol. **49**, 5529–5546 (2004).

[37]R. Amini, J. Z. Kartchner, L. A. Stolz, D. Biffar, A. J. Hamilton, and S. Adhikari, "A novel and inexpensive ballistic gel phantom for ultrasound training," World J. Emerg. Med. **6**(3), 225 (2015).

[38]B. Meirza, "Development of vessel phantoms for ultrasound methods," Masters thesis, Lund University, Lund, Sweden, 2018.

[39]M. O. Culjat, D. Goldenberg, P. Tewari, and R. S. Singh, "A review of tissue substitutes for ultrasound imaging," Ultrasound Med. Biol. **36**, 861–873 (2010).

[40]C. K. McGarry, L. J. Grattan, A. M. Ivory, F. Leek, G. P. Liney, Y. Liu, P. Miloro, R. Rai, A. P. Robinson, A. J. Shih, B. Zeqiri, and C. H. Clark, "Tissue mimicking materials for imaging and therapy phantoms: A review," Phys. Med. Biol. **65**(23), 23TR01 (2020).

[41]S. R. Guntur and M. J. Choi, "An improved tissue-mimicking polyacrylamide hydrogel phantom for visualizing thermal lesions with high-intensity focused ultrasound," Ultrasound Med. Biol. **40**(11), 2680–2691 (2014).

[42]G. Menikou and C. Damianou, "Acoustic and thermal characterization of agar based phantoms used for evaluating focused ultrasound exposures," J. Ther. Ultrasound **5**, 14 (2017).

[43]A. Eranki, A. S. Mikhail, A. H. Negussie, P. S. Katti, B. J. Wood, and A. Partanen, "Tissue-mimicking thermochromic phantom for characterization of HIFU devices and applications," Int. J. Hyperthermia **36**(1), 517–528 (2019).

[44]C. Lafon, V. Zderic, M. L. Noble, J. C. Yuen, P. J. Kaczkowski, O. A. Sapozhnikov, F. Chavrier, L. A. Crum, and S. Vaezy, "Gel phantom for use in high-intensity focused ultrasound dosimetry," Ultrasound Med. Biol. **31**(10), 1383–1389 (2005).

[45]B. Dunmire, J. C. Kucewicz, S. B. Mitchell, L. A. Crum, and K. M. Sekins, "Characterizing an agar/gelatin phantom for image guided dosing and feedback control of high-intensity focused ultrasound," Ultrasound Med. Biol. **39**(2), 300–311 (2013).

[46]R. L. King, Y. Liu, S. Maruvada, B. A. Herman, K. A. Wear, and G. R. Harris, "Development and characterization of a tissue-mimicking material for high-intensity focused ultrasound," IEEE Trans. Ultrason. Ferroelectr. Freq. Control **58**(7), 1397–1405 (2011).

[47]P. Blanc-Benon, B. Lipkens, L. Dallois, M. F. Hamilton, and D. T. Blackstock, "Propagation of finite amplitude sound through turbulence: Modeling with geometrical acoustics and the parabolic approximation," J. Acoust. Soc. Am. **111**, 487–498 (2002).

[48]S. Taghizadeh, C. Labuda, and J. Mobley, "Development of a tissue-mimicking phantom of the brain for ultrasonic studies," Ultrasound Med. Biol. **44**, 2813–2820 (2018).

[49]D. F. Leotta, R. E. Zierler, K. Sansom, A. Aliseda, M. D. Anderson, and F. H. Sheehan, "Evaluation of examiner performance using a duplex ultrasound simulator. Flow velocity measurements in dialysis access fistula models," Ultrasound Med. Biol. **44**, 1712–1720 (2018).

[50]D. F. Leotta and R. W. Martin, "Three-dimensional ultrasound imaging of the rotator cuff: Spatial compounding and tendon thickness measurement," Ultrasound Med. Biol. **26**, 509–525 (2000).

[51]D. F. Leotta and B. W. Starnes, "Custom fenestration templates for endovascular repair of juxtarenal aortic aneurysms," J. Vasc. Surg. **61**, 1637–1641 (2015).

[52]M. A. Ghanem, A. D. Maxwell, W. Kreider, B. W. Cunitz, V. A. Khokhlova, O. A. Sapozhnikov, and M. R. Bailey, "Field characterization and compensation of vibrational nonuniformity for a 256-element focused ultrasound phased array," IEEE Trans. Ultrason., Ferroelect., Freq. Control **65**, 1618–1630 (2018).

[53]P. B. Rosnitskiy, P. V. Yuldashev, and V. A. Khokhlova, "Effect of the angular aperture of medical ultrasound transducers on the parameters of

J. Acoust. Soc. Am. **151** (5), May 2022

Peek *et al.* 3017

nonlinear ultrasound field with shocks at the focus," Acoust. Phys. **61**, 301–307 (2015).

[54]G. P. Thomas, T. D. Khokhlova, Y. N. Wang, S. Totten, G. R. Schade, O. A. Sapozhnikov, and V. A. Khokhlova, "*In vivo* phase aberration correction for high intensity focused ultrasound therapy with a 256-element spiral array," J. Acoust. Soc. Am. **150**(4), A86 (2021).

[55]O. V. Bessonova, V. A. Khokhlova, M. S. Canney, M. R. Bailey, and L. A. Crum, "A derating method for therapeutic applications of high intensity focused ultrasound," Acoust. Phys. **56**, 354–363 (2010).

[56]F. Duck, *Physical Properties of Tissue* (Academic, Cambridge, 1990).

[57]T. D. Khokhlova, W. L. Monsky, Y. A. Haider, A. D. Maxwell, Y. N. Wang, and T. J. Matula, "Histotripsy liquefaction of large hematomas," Ultrasound Med. Biol. **42**, 1491–1498 (2016).

[58]T. Koch, S. Lakshmanan, S. Brand, M. Wicke, K. Raum, and D. Morlein, "Ultrasound velocity and attenuation of porcine soft tissues with respect to structure and composition: II. Skin and backfat," Meat Sci. **88**, 67–74 (2011).

[59]F. Shahidi, *Bailey's Industrial Oil and Fat Products. Edible Oil and Fat Products: Chemistry, Properties, and Health Effects* (Wiley, New York, 2005).

[60]T. Koch, S. Lakshmanan, S. Brand, M. Wicke, K. Raum, and D. Morlein, "Ultrasound velocity and attenuation of porcine soft tissues with respect to structure and composition: I. Muscle," Meat Sci. **88**, 51–58 (2011).

[61]L. Adamczak, M. Chmiel, T. Florowski, D. Pietrzak, M. Witkowski, and T. Barczak, "Using density measurement on semispinalis capitis as a tool to determinate the composition of pork meat," Food Anal. Methods **11**, 1728–1734 (2018).

3018   J. Acoust. Soc. Am. **151** (5), May 2022

Peek *et al.*